DOE/BC/15207-3

(OSTI ID: 807247)

Experimental Investigation of Relative Permeability Upscaling from the Micro-Scale to the Macro-Scale

Semi-Annual Progress Report

Reporting Period Start Date: August 1, 2001
Reporting Period End Date: Feb 28, 2002

Laura J. Pyrak-Nolte, JiangTao Cheng, Ping Yu, Nicholas Giordano, Mirela Mustata , Daiquan Chen, John Coy, Nathan Cooper, and David D. Nolte

April 2002

DOE Award: DE-AC26-99BC15207

Purdue Research Foundation
Department of Physics
1396 Physics Building, Room 166
West Lafayette, Indiana 47907-1396

Abstract: The principal challenge of upscaling techniques for multi-phase fluid dynamics in porous media is to determine which properties on the micro-scale can be used to predict macroscopic flow and spatial distribution of phases at core- and field-scales. The most notable outcome of recent theories is the identification of interfacial areas per volume for multiple phases as a fundamental parameter that determines much of the multi-phase properties of the porous medium. A formal program of experimental research was begun to directly test upscaling theories in fluid flow through porous media by comparing measurements of relative permeability and capillary-saturation with measurements of interfacial area per volume. During this reporting period, we have shown experimentally that the optical coherence imaging system can acquire information on grain interfaces and void shape for a maximum depth of half a millimeter into sandstone. The measurement of interfacial area per volume (IAV), capillary pressure and saturation in two dimensional micro-models structures has shown the existence of a unique relationship among these hydraulic parameters for different pore geometry. The measurement of interfacial area per volume on a three-dimensional natural sample, i.e., sandstone, has shown the homogeneity of IAV with depth in a sample when the fluids are in equilibrium.

Table of Contents

List of Figures

List of Tables

Executive Summary

Direct experimental tests of upscaling theories in fluid flow through porous media will be made by comparing measurements of relative permeability and capillary-saturation with measurements of interfacial area per volume. These experiments are performed from the pore-scale (microns) to the core-scale (centimeters), spanning four orders of magnitude in size. Three experimental objectives provide the data for rigorous tests of upscaling theories. First, holographic laser imaging techniques will acquire pore-scale three-dimensional optical images of the pore geometry in reservoir sandstones. This technique uses unique properties of coherent light to see through drilling muds and into the sandstone. Second, laboratory micro-models with matched topological properties based on the data from the pore imaging will make it possible to measure interfacial area per volume in scientifically controlled imbibition and drainage experiments, combined with measurements of capillary-pressure-saturation data and relative permeability. Third, core-scale experiments of relative permeability and capillary-saturation, and metal casts of the pore geometry, will be compared with the pore-scale data of the first two objectives. The data from all these objectives will provide the first complete picture over such a large dynamic range. It will make it possible to answer the principal question concerning flow upscaling: which microscopic measurements are most useful for predicting macroscopic flow properties of an oil reservoir. The tangible outcome of this work will be explicit data connecting interfacial areas, or other relevant geometric micro-scale data, with macroscopic hydraulic properties. In addition, we show strong industrial interest in testing and commercializing the unique down-hole laser imaging technology that can be transferred to the oil-industry service-company sector.

During this reporting period, we have shown experimentally that the optical coherence imaging system can acquire information on grain interfaces and void shape for a maximum depth of half a millimeter into sandstone. The measurement of interfacial area per volume (IAV), capillary pressure and saturation in two dimensional micro-models structures has shown the existence of a unique relationship among these hydraulic parameters for different pore geometry. The measurement of interfacial area per volume on a three-dimensional natural sample, i.e., sandstone, has shown the homogeneity of IAV with depth in a sample when the fluids are in equilibrium.

1.0 Introduction

1.1 Summary of Project Description

Standard expressions of multi-phase flow in porous media based on modifications of Darcy's Law (Darcy, 1856) have crippling deficiencies that make them undesirable to use for critical operations such as tertiary recovery of oil from depleted reservoirs. The primary difficulty in these empirical expressions are their violation of rigorous conservation laws. New theories based on rigorous volume averaging theorems and fundamental thermodynamic principles of phase boundaries have emerged in the past decade to replace the old empirical rules (Hassanizadeh and Gray, 1979; Gray, 1983). The most notable outcome of these theories is the identification of interfacial areas per volume for multiple phases as fundamental parameters that determine much of the multi-phase properties of the porous medium (Muccino, Gray and Ferrand, 1998).

Interfacial areas per volume provide natural descriptions of fundamental physical processes in porous media. For instance, thermodynamic energies are proportional to interfacial areas, and interfacial areas per volume represent a form of energy density. Gradients in energy densities define the dynamical pressures that drive the movement and distribution of phases within a complex topology. Interfacial areas per volume in a porous medium therefore represent a three-dimensional potential energy landscape.

Interfacial areas per volume also provide a natural yard-stick for defining the role of scale in multiphase fluid properties. The dimensional units of interfacial area per volume is a spatial frequency (inverse length) that breaks scale invariance. A useful illustration (Gray, 1998) of this scale-defining role can be made by considering an image of a pore-geometry containing only a single phase. Without a measurement scale, it is impossible to state what the physical size of the system is. However, when two phases such as water and air are both

present, the length scale becomes obvious. At small scales, the water-air interface is drawn into the pore throats, while at large scales the water puddles in the large void volumes.

Therefore, the interfacial areas between phases define a length scale. Whenever a physical system has an intrinsic length scale, the physics of the system can be divided into two regimes: one where sample sizes are larger than the intrinsic length scale, and the other where information is obtained on scales smaller than the intrinsic length scale. Breaking scale invariance makes it possible to define representative elementary volumes (REV) and to apply averaging theorems. Combining the averaging theorems with thermodynamics further constrains the possible types of constitutive equations that can rigorously describe multiphase fluid properties in porous media.

As a consequence of this theoretical framework, interfacial areas per volume (IAV) take on a more important role than simple volume saturation . This important role of IAV is clear because a single value of relative volume saturation can correspond to infinitely different distributions of two phases within the volume. Large values of IAV relate to a finely distributed phase that can block pore throats and seriously affect permeability, while small values of IAV relate to gross separations of phases, with large connected volumes of the phase that can flow unimpeded through the network. Significant numerical studies have been performed on the relationships between capillary-saturation and interfacial area. Reeves and Celia (1996) developed a numerical model that scans over repetitive imbibition and drainage while tracking the interfacial area for each loop. These studies pointed to a non-unique relationship between interfacial area and partial saturation, although a family of curves did emerge that lies within a localized part of the parameter space defined by area and saturation.

The numerical studies illustrate the importance of continued and extensive experimental studies and tests of upscaling theories, and in particular tests of the role of interfacial area per volume in determining macroscopic flow properties. While oil recovery predictions should certainly include IAV as critical parameters, it is important to test whether other microscopic

parameters also contribute to the macroscopic behavior. For instance, scale invariance of interfacial areas, even over restricted length scales, could present serious challenges to the averaging theorems, and could modify the presumed role of interfacial area in determining macroscopic flow properties. The principal objective of our proposed upscaling approach is to experimentally measure many microscopic geometric parameters of the flow system over many scales, and connect these microscopic measurements with macroscopic flow behavior.

1.2 Project Objectives

The proposed work for this contract has three objectives that will provide rigorous experimental tests of upscaling theories. The objectives are:

1) To use holographic laser imaging techniques to acquire pore-scale three-dimensional optical images of the pore geometry in reservoir sandstones. This technique uses unique properties of coherent light to see through drilling muds and up to a millimeter into the sandstone. This data forms the basis of upscaling experiments to test theories of interfacial area per volume.

2) To construct laboratory micro-models with matched topological properties based on the data from the pore imaging. Interfacial area per volume will be measured directly in controlled imbibition and drainage experiments, together with capillary-pressure-saturation data and relative permeability data. This set of interrelated data will allow rigorous testing of upscaling theories.

3) To perform core-scale experiments of relative permeability and capillary-saturation, and to make metal casts of the pore geometry and interfacial area per volume. This core-scale data (including pore-scale from the metal casts) will be compared with the pore-scale data of the first two objectives, extending the observation scales over four orders of magnitude.

2.0 Experimental

2.1 Optical Coherence Imaging

2.1.1 Experimental Set-up

An Optical Coherence Imaging (OCI) system was developed for this project to image into the sandstone. The OCI system (Figure 1) consists of a mode-locked Ti:sapphire laser (120 femtoseconds (fs) pulses with 100 MHz repetition rate), a modified Mach Zehnder interferometer with a sample arm and a reference arm, and a photorefractive multiple quantum well (PRQW) device[Nolte, D.D., 1999] that is the dynamic holographic film. An electric field (DC 10 kV/cm) is applied in the plane of the device. This configuration is called the transverse-field geometry that uses the Franz-Keldysh effect. In the interferometer, a de-magnified telescope (4:1) is used in the detecting arm that decreases the beam diameter to 1.0 mm on the sample. As a result, the intensity increases about 16 times at the sample. Two lenses with the same 150 mm focal length are separated by twice the focal length to form a 4-F system prior to the PRQW device (Figure 2).

In this 4-F system, the sample is placed at the focal plane in front of the first lens and the PRQW device is placed at the focal plane in back of the second lens (Figure 2). The plane that is halfway between the lenses is called the Fourier plane or the transform plane. The 4-F system projects a 1:1 image of the sample onto the holographic film. A spatial filter is located at the Fourier plane of the 4-F system to reject part of the scattered light from the sample, and allow the ballistic components to travel to the device. The signal beam interferes with the reference beam when the optical path lengths between the signal and reference arms are matched to within a coherence length of the laser by adjusting the translation stage in the reference arm. The interference fringes are imprinted onto the holographic film. The holograms are reconstructed using a degenerate four-wave mixing configuration. The first-order diffracted signal from the reference beam is imaged onto the surface of a cooled CCD camera (RTE/CCD 1317, Princeton Instruments) with a 150 mm focal length lens, while an

aperture is used to cut off the zero order beam. The efficiency of the four-wave mixing is optimized by adjusting the wavelength and bandwidth of the laser, the size and position of the aperture, and the relative intensities between the signal and reference beams.

To obtain information from deep in the sandstone, the system must be sensitive enough to acquire weak images under highly incoherent background. According to our theoretical analysis, the intensity of the first-order diffraction used to get a hologram in degeneration four-wave mixing can be increased by increasing the reference intensity. However, two limitations must be considered in the experiments when increasing the reference intensity. The first limitation is related to the Joule heating limit of the PRQW device that limits the total intensity on the device. We measured the Joule heating limit intensity to be about 90 mW/cm^2 for the device used in this project. In the experiments during this work period, a total intensity of 60 mW/cm^2 was used. The second limitation is the saturation of the cooled CCD camera caused by scattered light from the edges of the device and scattering defects in the device itself. To reduce the effect of the second limitation, the signal beam can be positioned on the device in regions with fewer scattering defects and edge effects. The signal beam has a diameter of about 0.5mm on the 1.0 mm device. The location of the signal beam can be selected using the region of interest (ROI) function of the cooled CCD camera. With this arrangement, uniform illumination across the entire device window can be achieved.

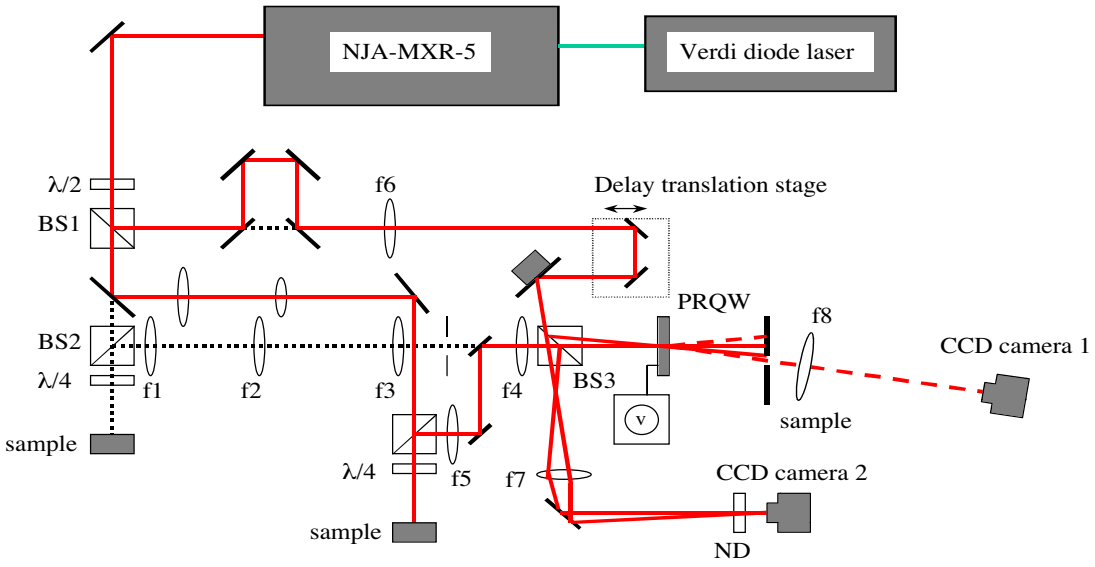

BS1, BS2: polarization beam splitter. BS3: 50/50 beam splitter.
f1=200mm, f2=100mm, f3=150mm, f4=f5=150mm, f6=500mm, f7=50mm, f8=150mm.
ND: Neutral Density Filter

Figure 1. The design and modifications of optical coherence imaging. The solid lines represent the modified setup and the dash lines are from the original setup.

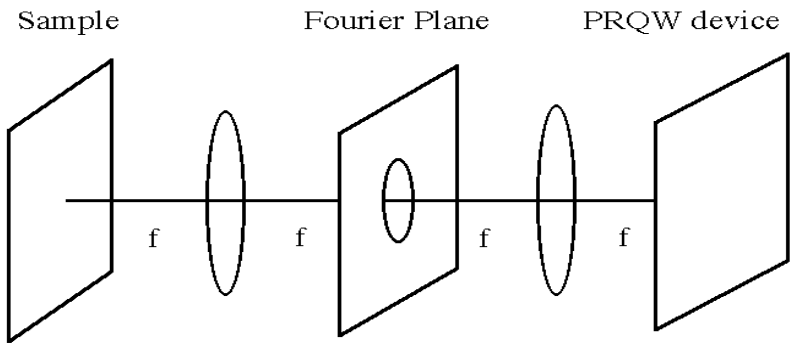

Figure 2. Two lenses form a 4-F configuration to get a 1:1 image between the sample and PRQW device.

2.2 MICRO-MODEL

2.2.1 Sample Preparation

This section gives a description of the procedures for performing optical lithography; complete details are given in the manufacturer's manual (Shipley, 1982) and by Thompson, Willson and Bowden (1994).

In optical lithography a pattern is transferred using a visible light image to a photo-sensitive polymer layer called photoresist. This layer acts essentially as photographic film. When a region of the photoresist is exposed to a sufficiently large integrated intensity of blue light, a photochemical reaction within the photoresist makes the region soluble in a special developer solution (usually just a base). The unexposed photoresist is not soluble, so after development the photoresist layer contains a negative image of the original light pattern. In all of our work we have used Shipley photoresist types 1805 and 1827, and their standard developer (Shipley, 1982). The image has been transferred to the photoresist in two different ways. In one method (Figure 3, left) a photomask is put in direct contact with the photoresist and the exposing light is transmitted through the mask. This mask is typically an opaque metal layer on a glass substrate, or a small portion of an ordinary video transparency sheet onto which the appropriate pattern has been printed. With this contact configuration the mask pattern is transferred in a 1:1 fashion to the photoresist sample; i.e., without magnification or reduction in size. We use this method for making the coarse (i.e., largest scale) features of the micro-models. The smallest sample features are made by projecting the mask pattern onto the photoresist through a microscope objective. We employ a specially modified optical microscope which enables the image of the mask to be focused onto the sample at the same time as the sample is in focus to the observer. Projecting through a 50x objective yields a 50:1 reduction in the size of the image relative to the scale of the mask. In this way we can routinely achieve sub-micron feature sizes at the sample.

Construction of a complete micro-model involves several steps (Figure 4). The first is to transfer the pattern of the desired flow geometry into a photoresist layer – this is accomplished using optical lithography as just described. The resulting glass substrate/photoresist layer will form the bottom and sidewalls of the final micro-model. The top wall (ceiling) of the micro-model is formed by a second glass coverslip. This "top plate" is bonded to the bottom layer using another layer of photoresist – this bonding is accomplished by bringing the two glass coverslips into contact with gentle pressure (approximately 1 atm, applied in a special holder in which a flexible plastic sheet is pulled against the sample by an applied vacuum) immediately after application of photoresist to the top plate (Figure 4a). The top plate also contains two holes (approximately 1 mm in diameter, drilled ahead of time) that serve as inlet and outlet for the finished micro-model (Figure 4c). The inlet and outlet regions are fairly open spaces (approximately 4 mm on a side) on the micro-model, and contain "pillars" which are approximately 0.5 mm in diameter to prevent collapse of the structure (Figure 4b). The working region of the micro-model is the area labeled as "channel" in Figure 4b. This is where a percolative pattern is created in the bottom photoresist layer.

2.2.2 Flow Measurement Apparatus

A schematic of the flow measurement apparatus for the micro-models is shown in Figure 5. This apparatus is used for simultaneous measurements of flow rate and optical characterization of the geometries of the various phases within the sample. This apparatus contains (1) two pressure sensors to monitor the input and output pressures, and (2) a video camera interfaced to an optical microscope to image the two-phase displacements experiments.

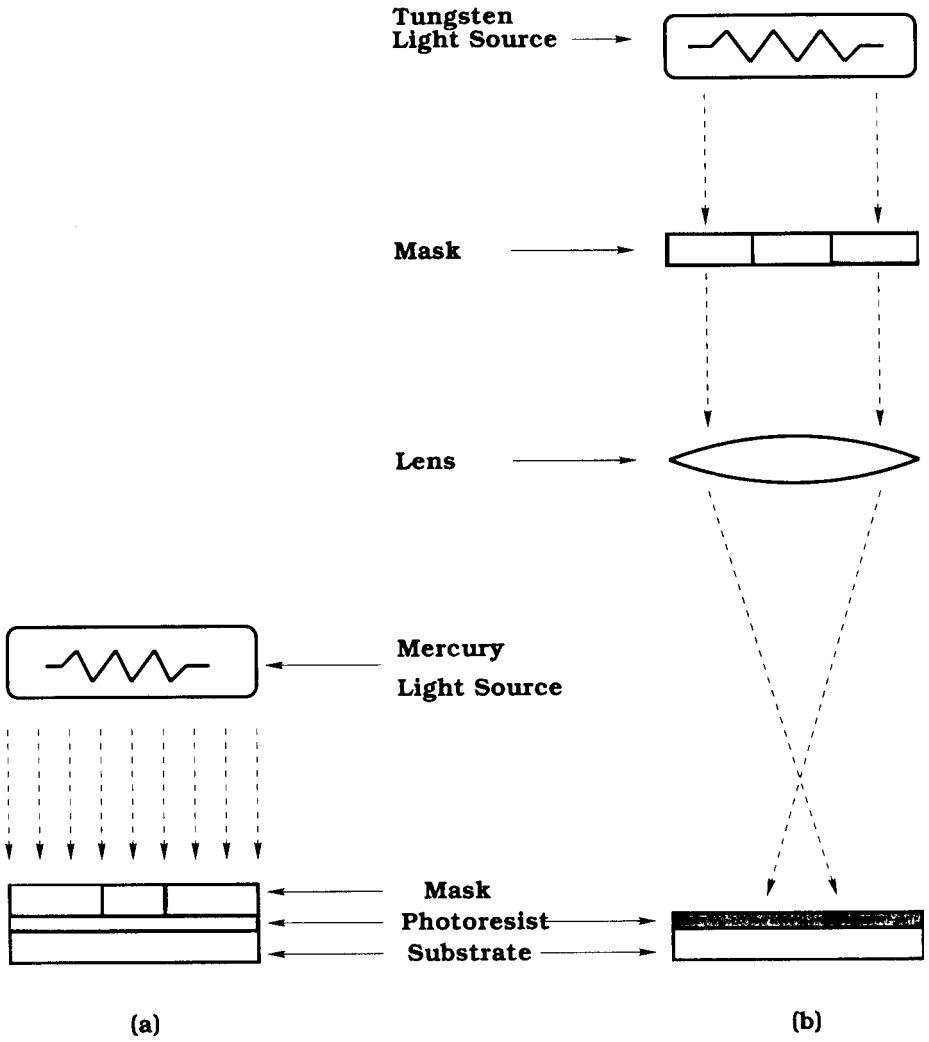

Figure 3. Schematics of the procedures used for optical lithography. Left: contact lithography. Right: projection lithography.

To perform a flow measurement on a micro-model, the micro-model is initially saturated with a fluid such as silicone oil, which is inserted through the "outlet" region in Figure 5. A second fluid, such as nitrogen gas, is then introduced through the inlet region. The flow rate of this second phase is measured using video microscopy together with an "on-chip" flow capillary. This capillary is a long narrow flow channel that is arranged to be in series with the sample and is located between the sample and the outlet region, as shown in Figure 6. The meniscus of the second fluid is tracked via microscopy as it moves along the

measurement capillary, and the flow rate calculated from the known dimensions of the capillary (typically 0.2 mm wide and 2.7 microns deep). This method makes it possible to measure extremely small flow rates very quickly. All measurements are conducted at room temperature (temperature stability better than 0.5 degree Celsius during a measurement), with the apparatus located within one of the clean bench environments.

The measurement of *IAV* is also accomplished with our video microscopy setup. For this we capture the image of the micro-model and do image processing with the computer interfaced to the camera. The captured image is processed using thresholding techniques to determine the areas occupied by both fluids and the interfacial area, both of which are crucial for our studies.

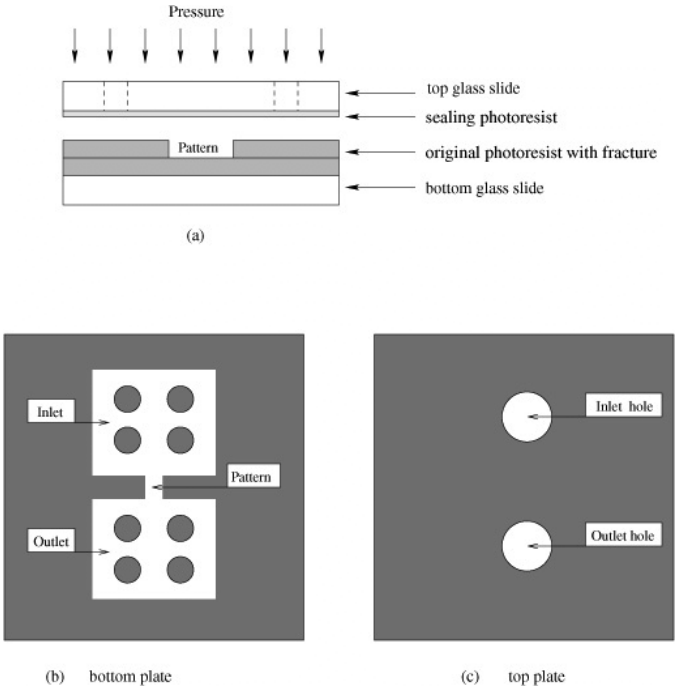

Figure 4. Micro-model layout. (a) Side view showing bottom plate containing micro-model pattern and top plate just prior to bonding. The glass slides are cover glasses 200 microns thick. The photoresist layers are 0.5 micron (type 1805 photoresist) and 2.7 microns (type 1827 photoresist). (b) Arrangement of inlet, outlet, and sample (channel) regions. (c) Inlet and outlet holes are drilled in the top plate.

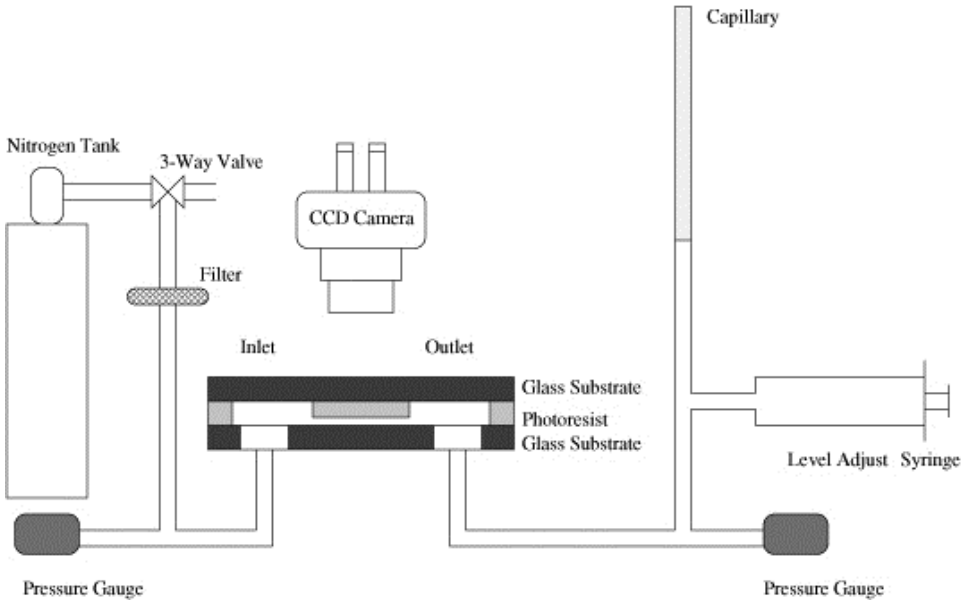

Figure 5. Apparatus used for measurement of flow rates and imaging of fluid geometry within a micro-model. The pressure sensors are piezoelectric sensors (model PX550C1 from Omega Engineering). The video camera system is a SPOT-1 RT color system (Diagnostic Instruments, Inc.) interfaced to a Macintosh G4 computer.

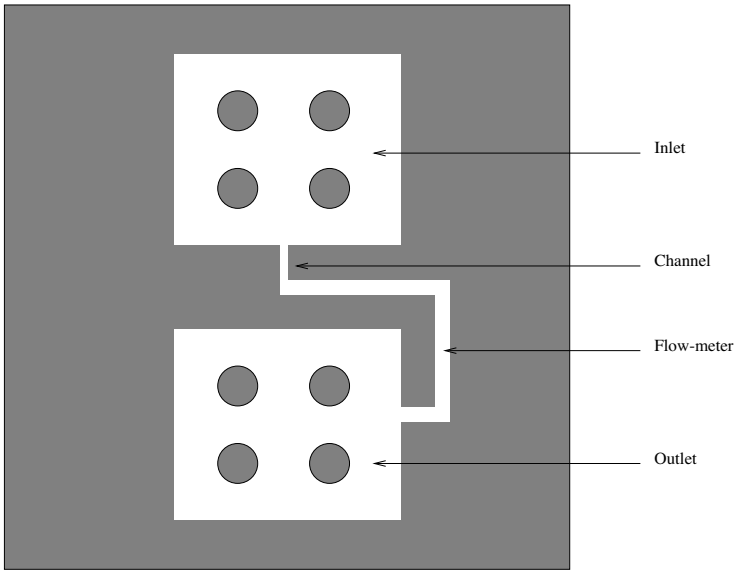

Figure 6. Micro-model with an "on-chip" capillary for the measurement of flow rates. The percolative flow structure is located in the region labeled “channel.”

2.3 Wood's Metal Injection

2.3.1 Sample Preparation Procedure

2.3.1.1 Sample Preparation for Injection & Flow Measurements

For the measurement of absolute flow rate and for the Wood's metal injection experiments, whole core samples from blocks of sandstone are used. The samples are cored to a diameter of 52 mm and have a length of 94 mm. The samples are coated with epoxy. The purpose of the epoxy is two-fold. First, the epoxy is used to increase the diameter of the sample by 52 mm to provide a competent sealing surface. The second purpose of the epoxy coat is to seal the surface pores of the sample to prevent dominant flow paths forming along the surface of the sample. The procedure for applying the epoxy coats includes: (a) applying a thin layer of epoxy to the surface the sample and letting the thin coat of epoxy harden; (b) placing the thinly coated sample in the center of a tube with a diameter of 104 mm; and (c) filling the remaining space in the tube with more epoxy and letting the epoxy harden. Measurement of the sample porosity is made prior to and after coating with epoxy using a wet/dry method.

2.3.1.2 Sample Preparation for IAV Measurements

After the sample has been injected and post-injection flow measurements have been made, the sample is destructively examined to obtain information on porosity, saturation of the sample with Wood's metal, and interfacial area per volume (IAV). The Wood's metal injected sandstone core is flushed with isopropyl alcohol to remove any remnant ethylene gylcol in the sample. The flushed sample is heated in the oven at a temperature of 54 °C for several days to evaporate the any remnant isopropyl alcohol. Then, the central portion of the sample is used for the investigation of IAV. The sample is cut to a 25.4 mm by 25.4 mm by

100 mm rectangular prism, and then sectioned into 4 pieces measuring approximately 25.4 mm by 25.4 mm by 25.4 mm. The size of the sample is controlled by the sample holder of the Scanning Electron Microscope (SEM). After cutting of the sample to the required size, the surfaces (perpendicular to the global flow direction during injection) of the four sections are polished on a polishing wheel (15 micron powder size) to create a flat polished surface.

2.3.2 SEM Scanning Procedure for Sandstone Samples

Using a Scanning Electron Microscope enables the collection very high magnification images of the pore space and metal-filled pore space in the sandstone samples. The SEM used for this project is a JEOL 35CF operated with an accelerating voltage 25kv, an objective aperture setting of #2, a working distance of 39 mm and a condesner lens current of 2.00 to 3.00.

To ignore topographic information from the SEM images, the SEM is operated in a point by point scanning mode using the backscattered (Backscatter Electron Image - BEI) and COMP mode settings. A slow scanning speed is used because the signal is weak and noisy. Digital images are collected with IMIX software installed in a computer, which is connected to the SEM.

The contrast in the resulting image is determined by the material type (atomic number) on the sample surface (Wood's metal, sandstone, air). In the initial testing, the sample was injected with epoxy after being injected with Wood's metal. The epoxy-filled portions of the pore space represented the location of the ethylene gylcol. For samples with a high saturation of Wood's metal, it became difficult to inject epoxy into the sample. The epoxy injection step of the procedure has been eliminated. This requires us to assume that any portion of the pore space not filled with Wood's metal would be filled by a wetting phase.

2.3.3 Wood's metal Injection Procedure

Wood's metal injection experiments were performed on several sandstone samples. The following procedure was used for Wood's metal injection experiments:

1. Place Wood's metal tank (Figure 7). Mount the sample in holder and install sample in the other tank and seal. Fill the holding tank with paraffin oil. Close valves 1, 2, 3, 4, and 5. Place flexible heaters on the outlet tubing leading to sample and the chamber on the tubing. Monitor the temperature and pressure of the whole system.
2. Increase the temperature of the paraffin oil to 90 °C. Once a temperature of 90 °C has been achieved, maintain the temperature four hours before Wood's metal injection.
3. Apply 137.9 kPa gas pressure to Wood's metal tank. Open valves 1 and 4. Open valve 2 to let melted metal flow into sample tank until the sample is completely covered by metal as indicated by the level detector.
4. Close valves 1 and 2. Heat the outlet tubing and chamber to around 90 °C.
5. Apply desired gas pressure to sample tank. Open valves 1 and 4 for metal injection. Use scale to monitor ethylene glycol flow rate. Adjust gas pressure during the injection to maintain a constant pressure. Turn off valve 1 when steady ethylene glycol flow is reached while maintaining the pressure in sample tank. Stop heating the outlet tubing and chamber.
6. Open valve 3. Open valve 2 to let metal flow from sample tank to Wood's metal tank while the pressure in sample tank is maintained at the desired value. Let the metal flow until the sample is not in contact with the metal (based on level detector).
7. Drain paraffin oil from the holding tank and let the system to cool down.
8. Relieve gas pressure when temperature is lower than 50 °C. Open sample tank and remove sample out for further experiments and measurements.

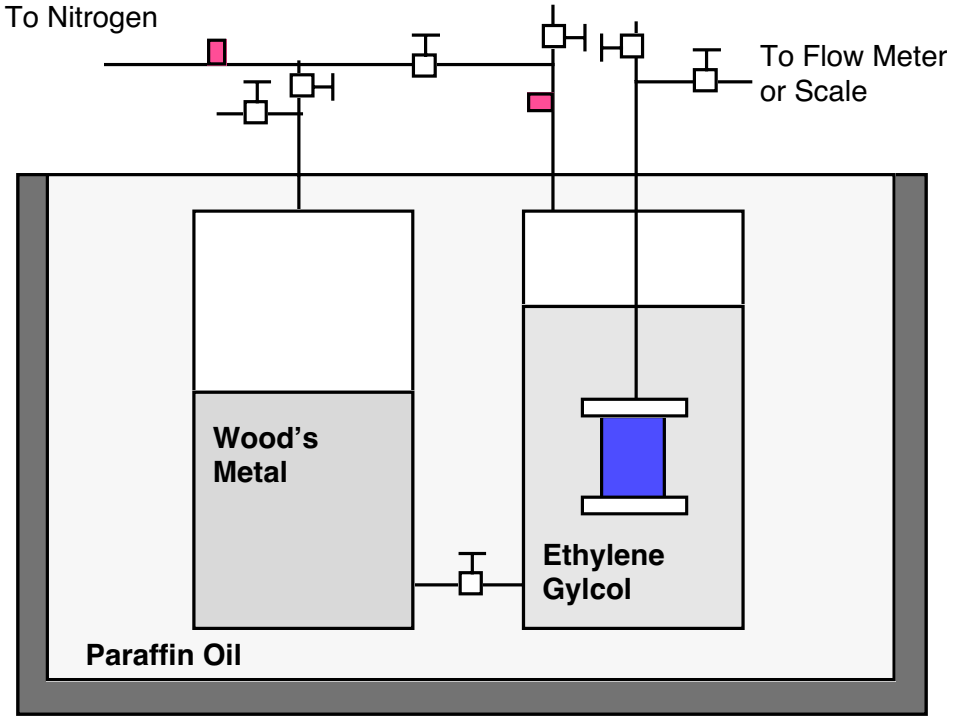

Figure 7. Schematic of Wood's metal injection system.

3.0 Results and Discussion

3.1 Optical Coherence Imaging

In our previous report, we demonstrated that Optical Coherence Imaging (OCI) successfully imaged to the back of the first layer of grains. An important goal of this work is to obtain information on the void spaces between grains by imaging deeper than the first layer of grains. With an improvement of experimental conditions that optimizes holographic recording and reconstruction to perform laser-ranging into sandstone, we have imaged several grain layers into a sandstone sample. Three-dimensional microscale information on grain size and geometry was obtained as deep as 500 microns into the sample.

Figure 8 shows the orientation of the sandstone sample in the OCI setup. We define a co-ordinate system in the sample where each acquired image is located in the x-y plane and cross-section holograms that are reconstructed from the 3D data cube is in the x-z plane. The input femtosecond laser propagates in the z direction. Figure 9 show a series of cross-section holograms with a distance of 12 μm in the y direction between image sequences. To better view the results, a rainbow pseudo-color is used show the intensity of the reflected signal from different locations within the sample. The dimensions of each image are 1.0 mm (lateral) × 1.0 mm (depth). Depth is along the horizontal axis and increases to the right in the images. The bright holograms come from the reflections off the grain facets. Weak reflections either come from deep grains or form tilted facets. Careful examination of the image sequence in Figure 9 shows that there is a pore structure near the sample surface marked with the white arrow. Although bright holograms appear to be seen at positions deeper than 800 μm, this depth is actually 500 μm in real space depth due to the refractive index of the sandstone. In Figure 10, two grains marked with red and green arrows in each frame can be seen clearly, which shows a possible structure with one grain behind another in depth. The areas outlined by the white dashed line in Figure 11 show several reflections with

large angles corresponding to tilted facets of the grains. Also, another pore structure marked with a white arrow is seen near the sample surface.

By looking for closely-spaced reflection peaks in the depth sections, it may be possible to measure the gaps between grains. An OCT hologram of sandstone is displayed in Figure 12(a). The hologram is a cross-section of a sandstone sample in x-z plane at y = 820 μm showing considerable structure down to 500 μm deep, extending through several grains at each position. Line sections at the location x = 75 μm and 156 μm are shown in Figure 12 (b). Reflections indicated by arrows from the top and the bottom of grains can be seen, as well as deeper reflections from deeper grains. Though it is not possible to determine the 3D structure from a single cross-section, the full data set contains sufficient information to fit the positions and shapes of numerous grains in the top several layers of grains in the sandstone sample.

We are currently extending the imaging system to allow saturation of the sandstone with water. Two facets bounding a void each produce reflections that are identical to the facets bounding a grain. But when water is introduced into the pore-space, the light time-of-flight through the now water-filled void increases, stretching the apparent distance between reflections. Therefore reflection doublets that stretch upon the addition of water to the pore space can be unambiguously identified as void spaces, while doublets that do not change are the grains.

Cross section holograms of the sandstone with and without water show a significant difference between the two experiments. Holograms are shown in Figure 13 to demonstrate the principle of the measurement. The dimensions of the frames are 1.0 mm (lateral) × 0.7 mm (depth). Figure 13 (a) and (c) are cross-section holograms from the sample with water while Figure 13 (b) and (d) are cross-section holograms from the sample without water. Straight bright lines can be seen in the x direction in Figure 13 (a) and (c). These lines are from the water surface reflection. The water surface reflection is strong compared to

reflections from the sandstone. We arrange the laser beam input in a direction tilted away from the vertical direction to minimize the surface reflection that can be cut off by a spatial filter. Only a small amount of the water reflection arrives at the device. It is important that the same regions are compared between the samples with and without water. The dashed lines in figure 13 (a) and (b) are from the top surface of the sandstone. We can see similarity between the frames. In figure 13 (c) and (d), two grains are outlined by a dashed square and solid square. The distance between the grains is changed due to the water. Therefore we can recognize a pore space between these grains.

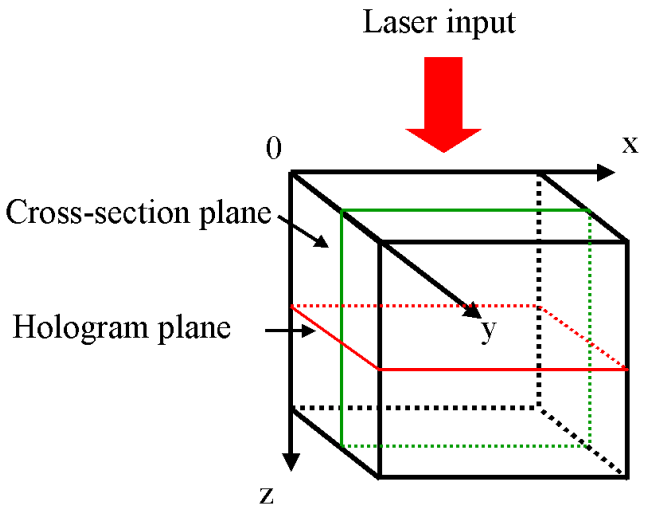

Figure 8. Orientation of the sample and measurement direction.

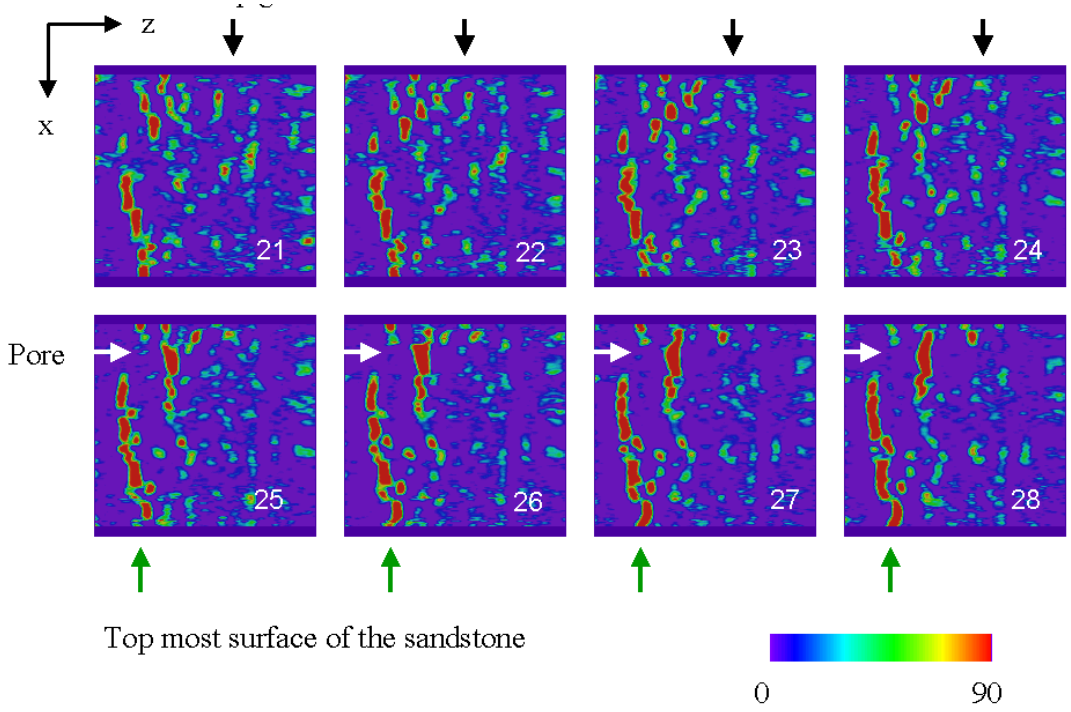

Figure 9. Cross-section holograms of sandstone. Frames are separated in the y direction with a distance of 12 μm. The dimensions of the frames are 1.0mm x 1.0 mm.

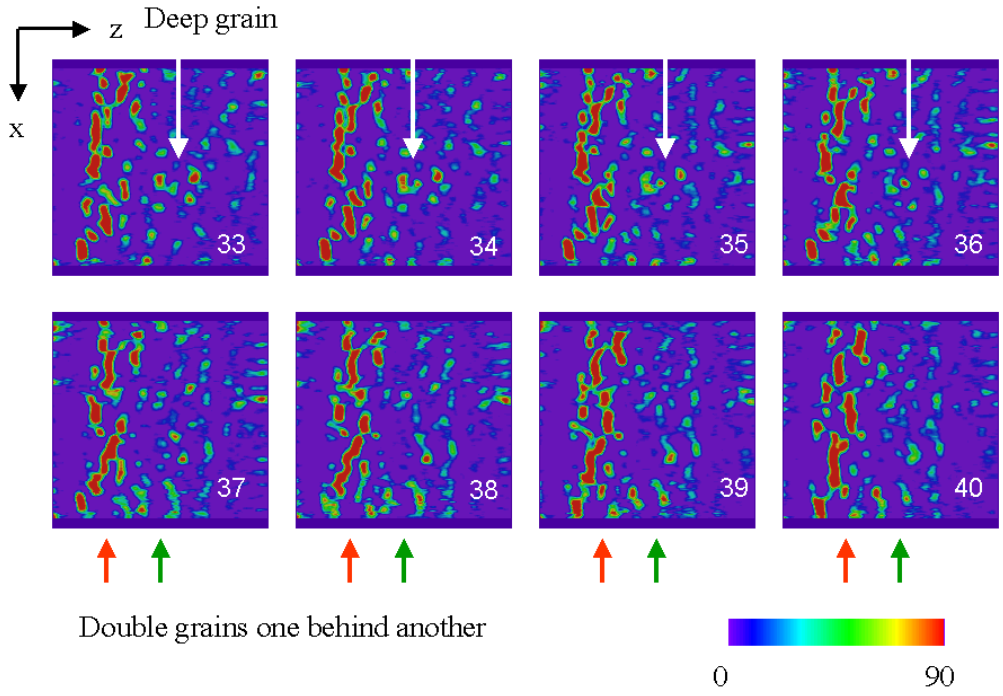

Figure 10. Cross-section holograms of sandstone. Frames separate in y direction with a distance of 12 μm. The dimensions of the frames are 1.0mm x 1.0 mm.

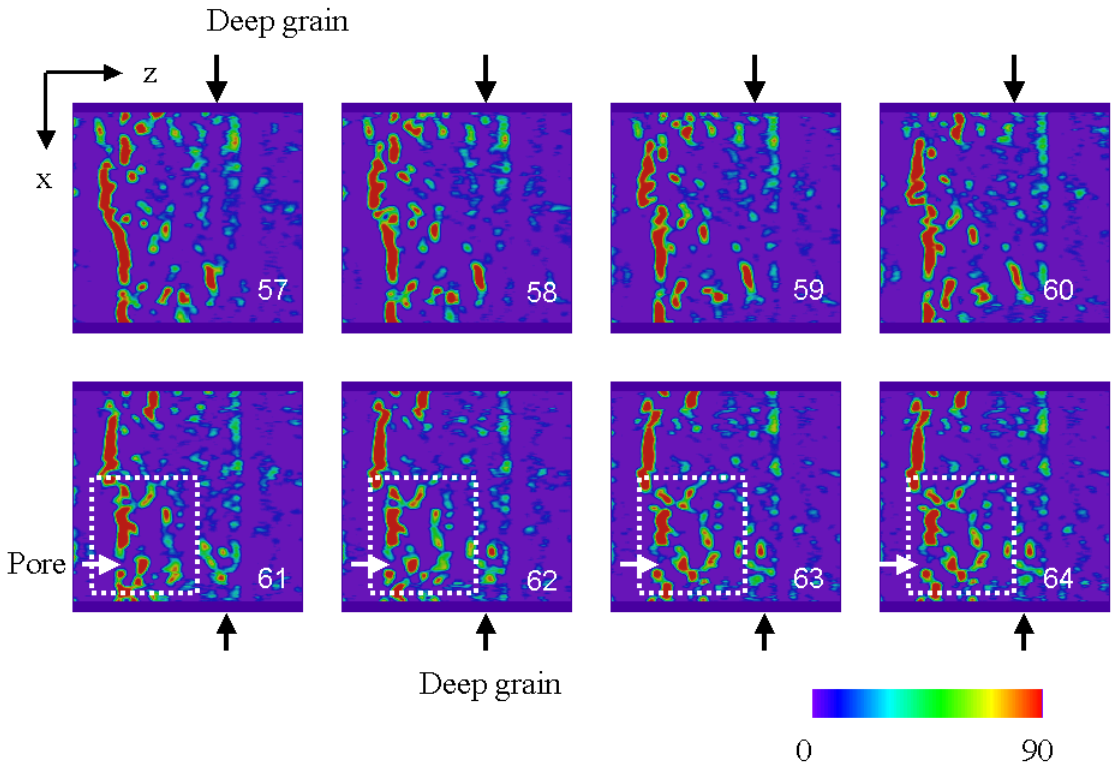

Figure 11. Cross-section holograms of sandstone. Frames separate in y direction with a distance of 12 μm. The dimensions of the frames are 1.0mm x 1.0 mm.

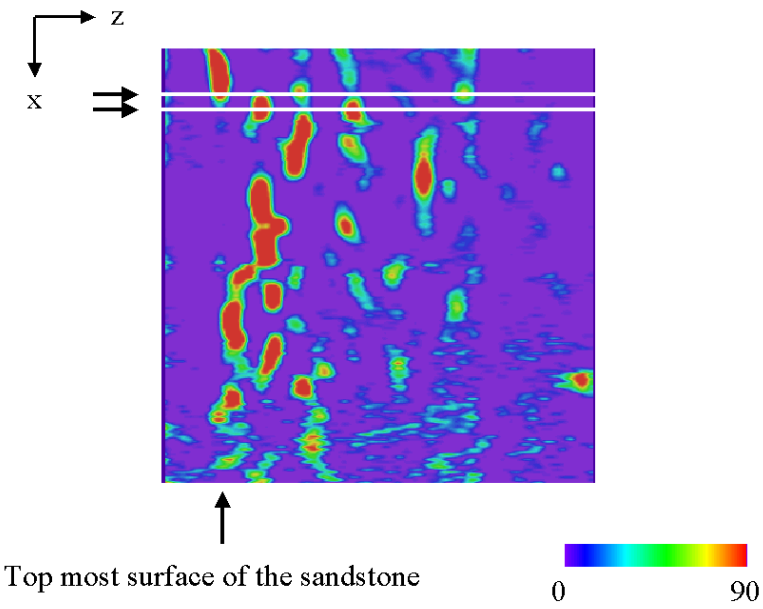

Figure 12 (a)

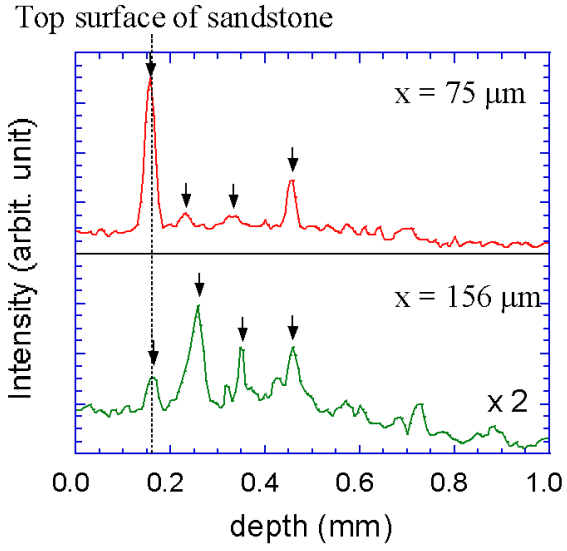

Figure 12 (b)

Figure 12 (a) Cross—section at location y=820 μm with dimensions 1.0 mm by 1.0 mm in the x-z plane, showing considerable structure half a millimeter deep into the sandstone sample. The bar represents the scale on both x and z axes. Marked lines show where the intensity cross sections of (b) were taken. (b) Intensity cross-section through 1.0 mm depth at x=75 μm and 156 μm.

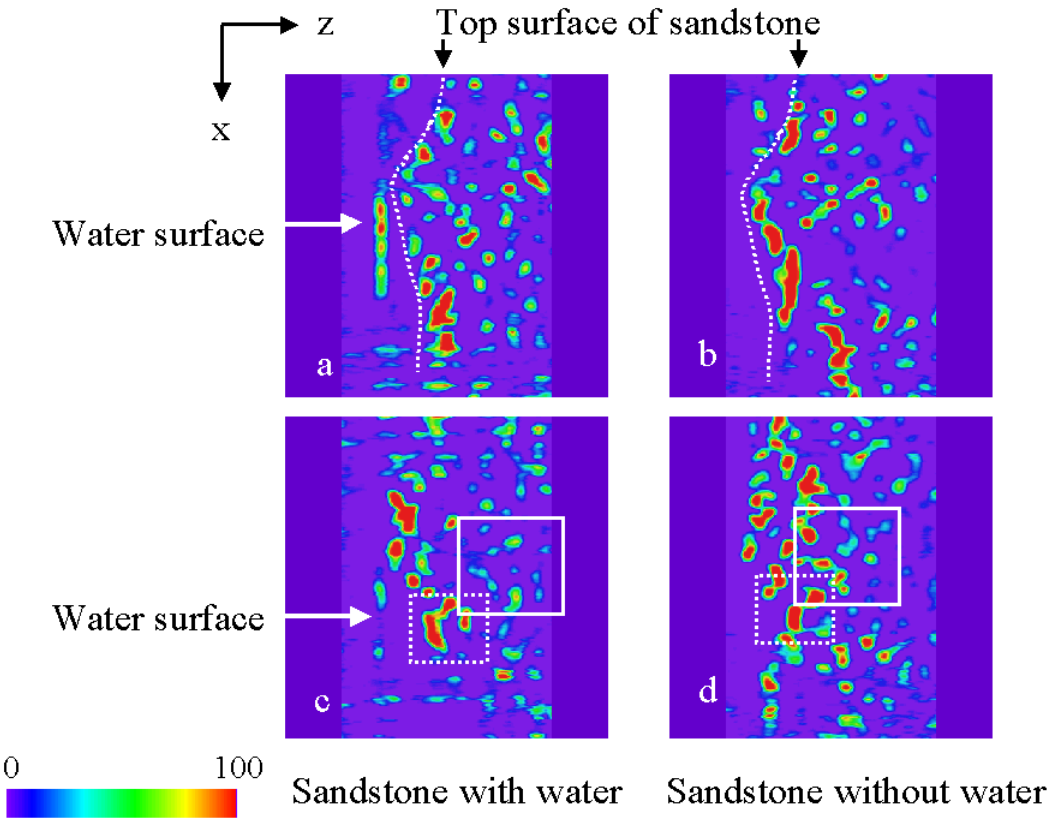

Figure 13. Cross section holograms of sandstone with (a), (c) and without (b), (d) water. The dimensions of the frames are 1.0 mm (lateral) x 0.7 mm (depth). Dashed lines are from the top most of the sandstone. Arrows show the reflection from water surface. Dashed and solid square marked two grains.

3.2 Micro-Models

Two types of micro-models have been fabricated and studied in detail. One type was designed using the five-tier multi-fractal patterns described by Nolte and Pyrak-Nolte (1991), while the other type employed one-tier patterns which by their nature are not multi-fractal (Nolte and Pyrak-Nolte, 1991). Figure 14 shows a series of photomicrographs showing the process of nitrogen gas displacing the liquid decane. Here the micromodel geometry is uncorrelated – i.e., non-hierarchical in the terminology of Nolte and Pyrak-Nolte (1991).

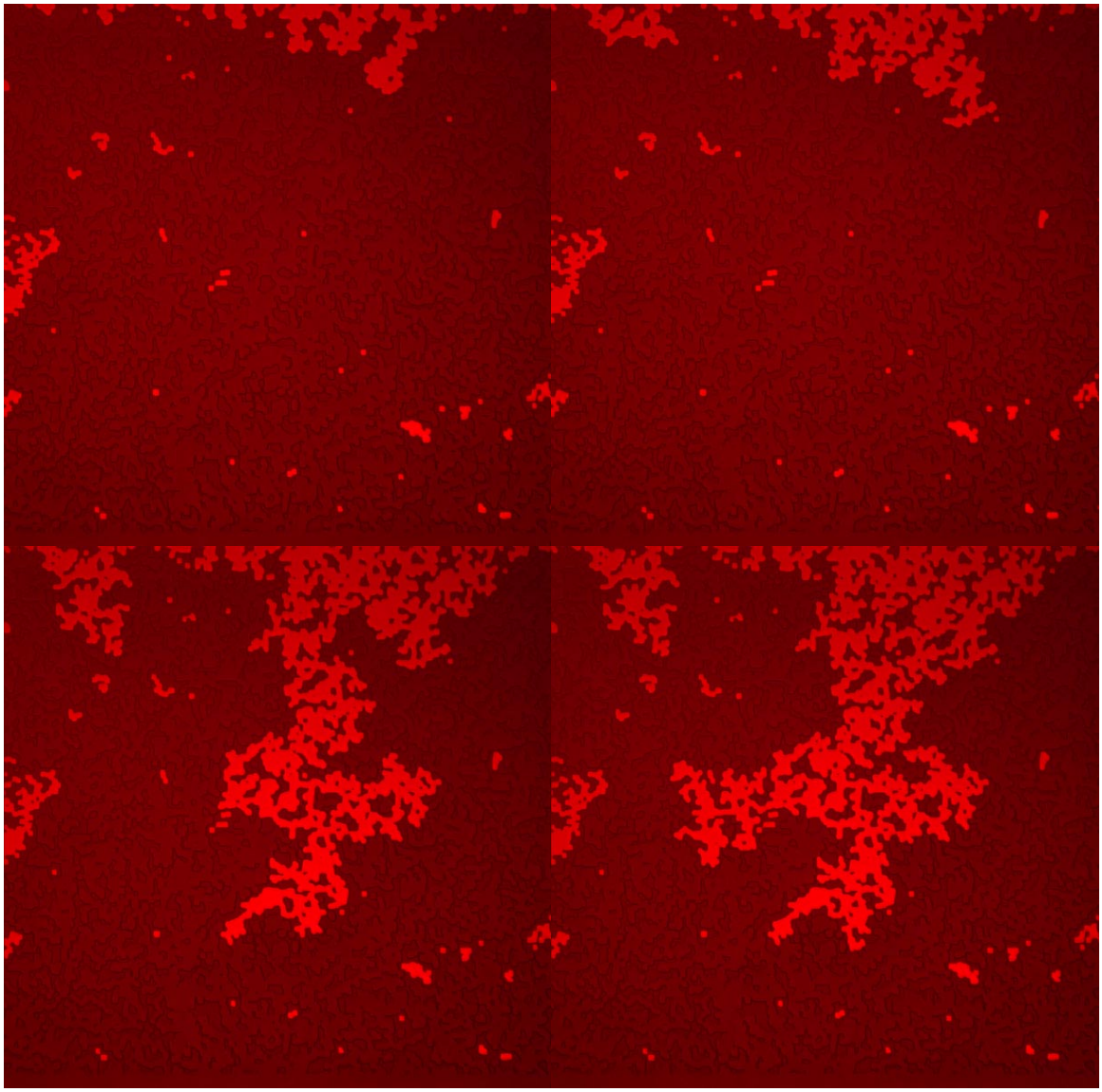

Figure 14. Photomicrographs of nitrogen gas (the brightest phase) as it displaces decane. The darkest regions are inaccessible to decane, while the phase of intermediate optical density is decane.

These results were obtained by first filling the sample with decane, then forcing in nitrogen gas (from the top of the photos) with a slight pressure. This pressure was then held fixed for 5 minutes (this was long enough to reach equilibrium – waiting longer produced no further changes) and a photograph was recorded. The pressure was then increased slightly and a new photograph recorded (after a 5 minute wait). The photos in Figure 14 show how

the nitrogen invaded as the pressure was increased from a low value (top left), in stages (proceeding to top right, bottom left, and then the bottom right photo).

As the gas pressure is increased, more and more of the liquid is expelled from the system. Eventually one reaches a point where further increases in the pressure make essentially no change in the liquid saturation. Note however, that some liquid may still be trapped in isolated pockets, as is clearly seen in Figure 14.

If the gas pressure is then reduced, liquid will reenter the system and displace the gas. This process of drainage-imbibition is a crucial element of multiphase flow. It can be viewed in a plot of capillary pressure (i.e., the gas pressure) versus fluid saturation. Several cycles of drainage-imbibition are shown in Figure 15.

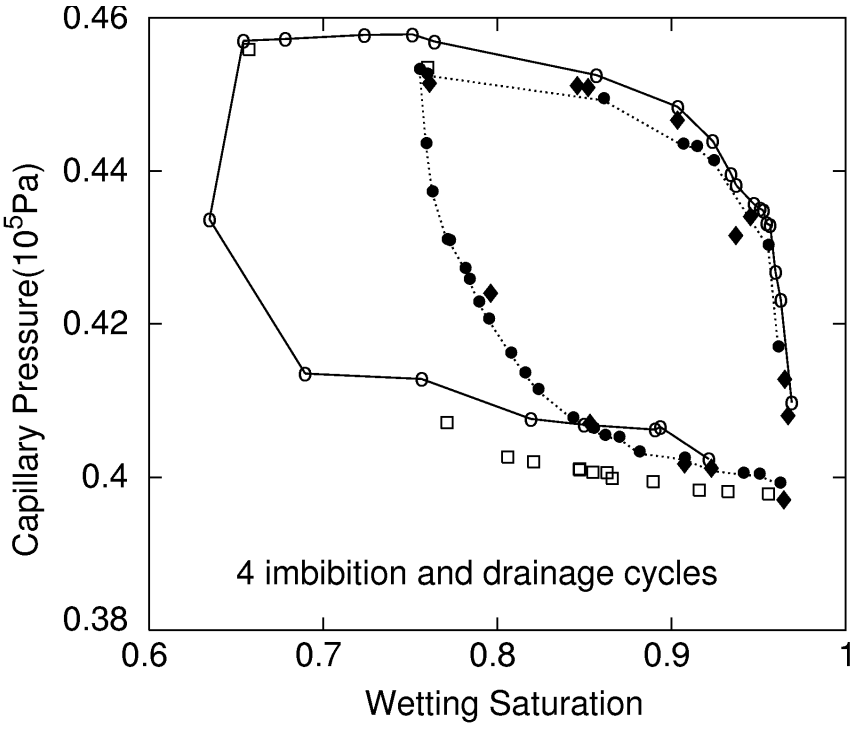

Figure 15. Drainage-imbibition cycles for the sample shown in Figure 14.

A striking feature of the drainage-imbibition process is that, as seen in Figure 15, the behavior is almost always hysteretic. That is, these cycles do not retrace as the pressure is increased/decreased. Different cycles are followed, depending on the speed with which the pressure is changed, the size of the pressure changes, etc. For this reason is it hard to formulate a "thermodynamic-like" theoretical description.

In the theory of Gray and coworkers a new variable immerges, which allows one to deal in a natural way with this hysteresis. That variable is the area of the interface which separates the liquid and gas phases. It is usually referred to as the interfacial area per unit volume (of the system), IAV; we will use the same term, even though our micromodels are two dimensional (so that we really have an interfacial line-length per unit area).

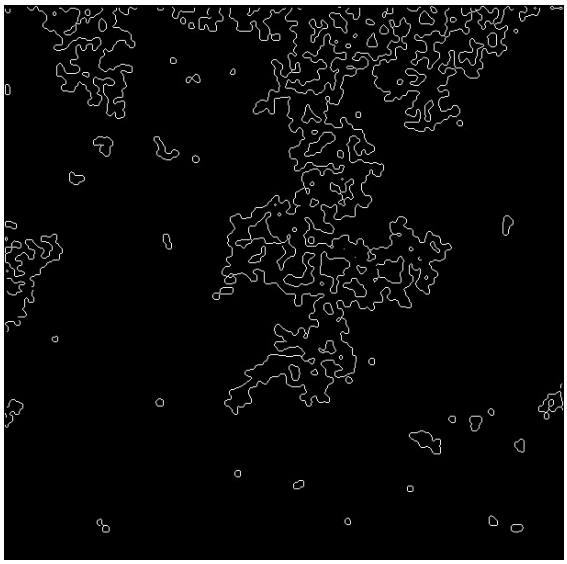

Figure 16. Gas-liquid interface from the lower left photo in Figure 14.

The experimental measurement of the IAV is very challenging. We have worked extremely hard to produce micromodels with very uniform optical density, so that the contrast between the different phases is very consistent across the sample. This has enabled us to use commercial image analysis software (IDL) to analyze images like those in Figure 14. Figure 16 shows the gas-liquid interface as extracted from one of the images in Figure

14. Results like those in Figure 16 have allowed us to measure the IAV during drainage-imbibition cycles like those shown in Figure 15. Some results for the IAV-Pcap-S surface are shown in Figure 17.

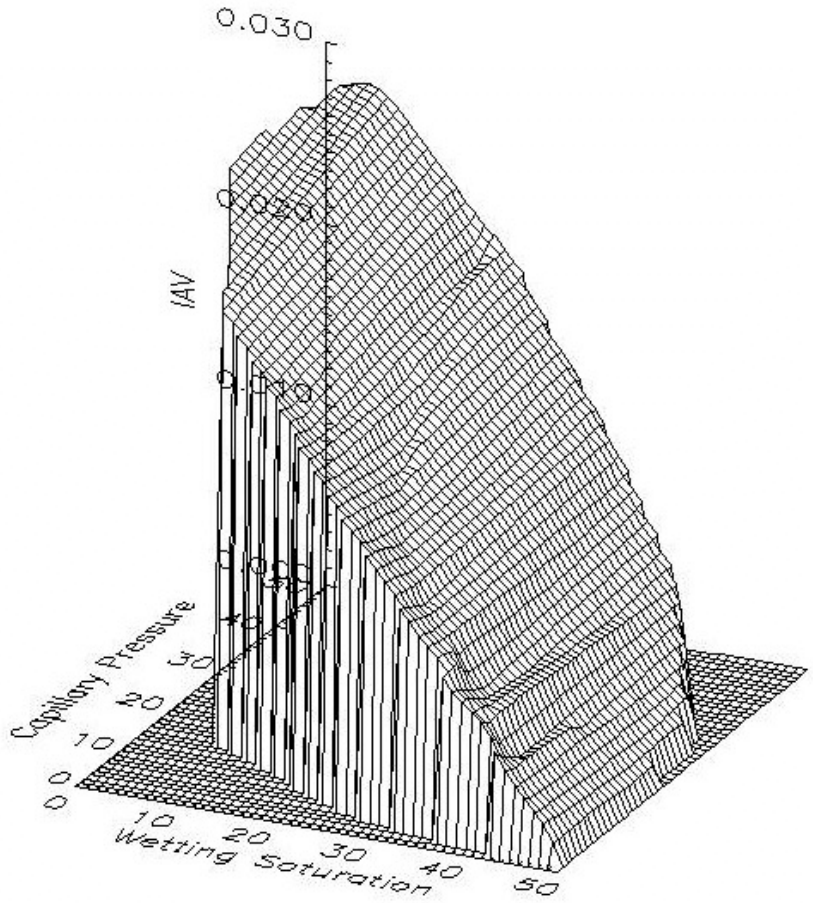

Figure 17. IAV-Pcap-S surface measured for the sample in Figure 14. P_{cap} and S are in the same range and in same units as in Figure 15, IAV is in unit of μm^{-1}. A wetting saturation value of 50 (in the arbitrary units used here) corresponds to a sample which is completely filled with decane.

The vertical "walls" in this plot are not regions where IAV changes abruptly; they merely indicate where the data set ends. The important point here is that the IAV- Pcap-S surface is

single valued. When viewed in this expanded space (including IAV) the hysteresis seen in Figure 15 vanishes. This is strong experimental evidence that these three variables are sufficient to describe and characterize multiphase flow. Figure 18 shows IAV-Pcap-S results for a micromodel with a correlated (multi-fractal) pore geometry. We are now in the process of studying the IAV surface for a variety of different samples so that we can determine how one can predict the nature of this surface as the pore geometry, pore size, etc., are varied.

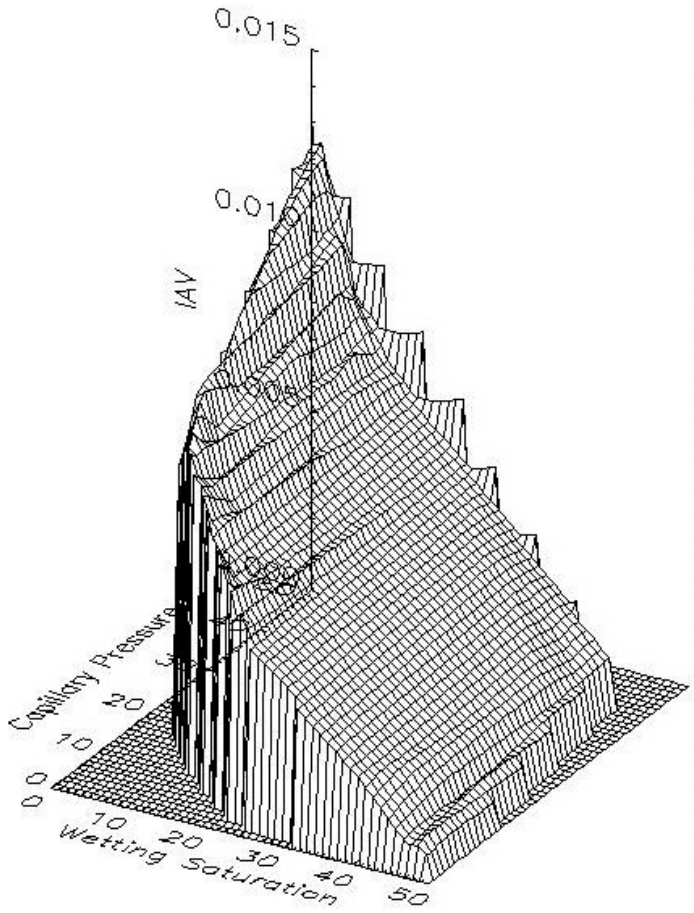

Figure 18. IAV-Pcap-S surface for a sample with a multi-fractal pore geometry. See Figure 17 for a description of the units.

Comparing the *IAV* surfaces in Figures 17 and 18 one notices that they are actually quite similar in form, and that the overall magnitude of *IAV* differs only by a factor of 2.

Similarities of the *IAV* surface from sample to sample, or even some sort of "universality" of this surface would be a very important and powerful result. With this in mind, we show in Figure 19 the *IAV* maximum value (obtained from data like that in Figures 17 and 18) as a function of the sample porosity (the fraction of the sample area which is accessible to fluid). The results here are for both correlated (multi-fractal) and uncorrelated pore geometries. It appears that the *IAV* maximum is rather constant, although it can vary from sample to sample. We are now trying to understand what features of the sample geometry influence the *IAV*.

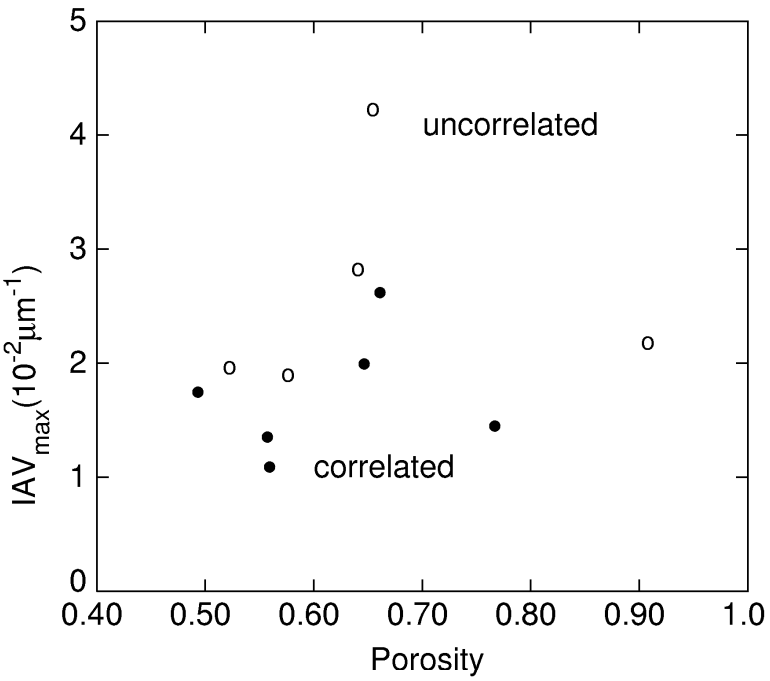

Figure 19. Maximum IAV value as a function of the sample porosity. Note that the symbols next to the terms "correlated" and "uncorrelated" are not data – they just indicate the notation.

3.3 Wood's Metal Method

A goal of the Wood's metal injection experiments is to acquire interfacial area per volume (IAV) data for sandstone cores. This requires destructive sectioning (see section 2.3.1.2) of the core after the sample has been injected with Wood's metal. To find reliable IAV values, images of the sample are needed from which the different phases filling the pore space can be discerned.

3.3.1 Image Analysis for IAV

After acquiring SEM images from the Wood's metal injected sandstone samples for several depths and locations, the images are processed to identified the various phases in the sample. A custom code is used to threshold the images for each of the phases. The number of phases is three (air-Wood's metal – sandstone, or Wood's-metal – epoxy – sandstone). First the saturation and the edge length of each phase, S1, S2, S3, L1, L2, L3 are obtained. Then based on the assumption that each phase contacts with either the second or the third phase, we can calculate L12, L13, L23, the edge length between every two phases following some simple relations:

$$L12=(L1+L2-L3)/2$$

$$L13=(L1+L3-L2)/2$$

$$L23=(L2+L3-L1)/2.$$

From our previous study performed under this contract, the error in the value of edge length from image analysis is 10 percent. In this report, all values of IAV reported for the sandstone samples will be shown with 10 percent error bars. The values of area fractions from image analysis are accurate to within one percent.

3.3.2 IAV Results

Unlike the micro-model experiments (see section 3.2), one Wood's metal experiment and the subsequent image analysis, produces one data point for the interfacial area per volume, saturation and capillary pressure curve. In the micro-model experiments, one experiment can produce a 100 points of data.

We analyzed the images obtained from Sample 5a to determine the homogeneity of IAV and porosity at a given depth and with depth in the sample. Homogeneity of the porosity indicates that the micro-structure of the sample does not vary significantly within a sample. Homogeneity of IAV with depth in a sample indicates that equilibrium was reached during the injection experiments. Figure 20 and 21 show the variation of porosity and interfacial length per area, respectively, determined from image analysis for one depth from sample 5a. The sum of the area fraction for the metal and air represent the porosity of the sample (Figure 20). For sample 5a which was subjected to an injection pressure of 0.34 MPa, the pore space is predominantly filled with metal. The porosity determined from the image analysis is listed in Table 1. The porosity is relatively constant for a given surface (Figure 20). However, the ILA tends to show a greater variation at a given depth as determined from the image analysis. The value of ILA for rock-metal and rock-air interfaces are of the same order of magnitude.

Figure 22 shows the variation in the ILA in sample 5a as a function of depth in the sample, i.e., the average value for each of the eight surfaces based on 10 images per surface. Assuming an error of 10% in the values of ILA from the image analysis, the average ILA values are uniform with depth in the sample. This is also true for the saturation of woods metal in the samples used in this investigation. Agrawal et al. (1991) observed a distribution of woods metal saturation with depth in a sample. They suggested that the distribution would be more uniform if the injection time was increased. For this project, the injection process is maintained until equilibrium is reached.

Figure 23 shows the variation in ILA as a function of injection pressure. Each pressure corresponds to a different sample (Table 1.). Assuming a 10% error in the measurement of ILA from image analysis, the value of ILA is almost independent of the injection pressure. This suggest that the pore size in the sample is relatively large compared to the estimated size of the minimum pore penetrated by the Wood's metal (Table 1). Additional experiments need to be performed at low injection pressures to reduce the amount of pore space filled with Wood's metal. However, a low injection pressure requires a time frame on the order of a month to reach equilibrium for a our current sample size. The homogeneity in ILA with depth in the samples suggests that the sample length can be reduced to accommodate low injection pressures and to reach equilibrium in a reasonable time frame.

Table 1. Porosity, injection pressure and estimated minimum pore size penetrated for each sample.

Sample number	1a	4a	5a	6a
Porosity from weight (%)	18.5	16.5	18.6	16.2
Porosity from image analysis (%)	20.4	20.6	20.4	19.8
Injection pressure (MPa)	0.10	0.17	0.34	0.034
Estimated minimum pore size penetrated (micron)	4.8	2.8	1.4	14

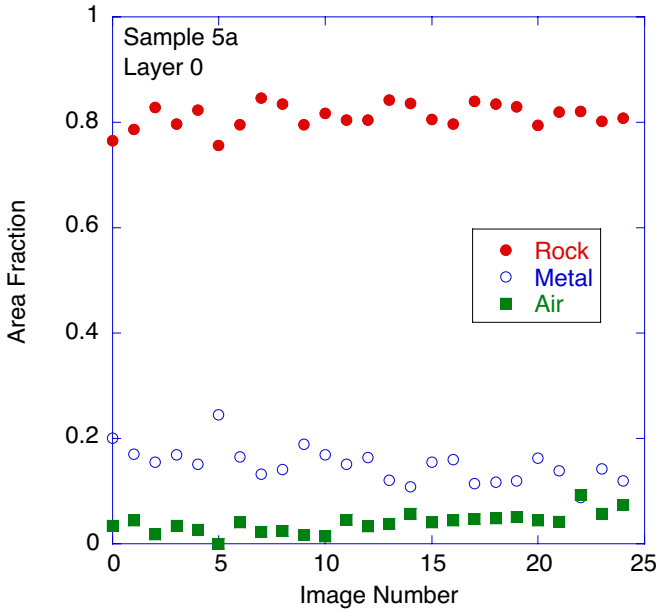

Figure 20. Area fraction of rock, metal and air for Sample 5a from depth position (layer) 0. The sum of the area fraction for the metal and air components is the porosity.

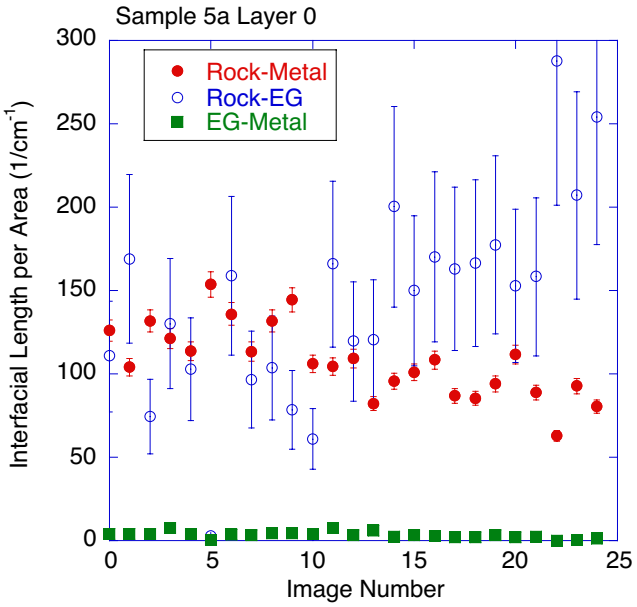

Figure 21. Interfacial length per area from sample 5a based on image analysis of 25 SEM micrographs from depth position (layer) 0.

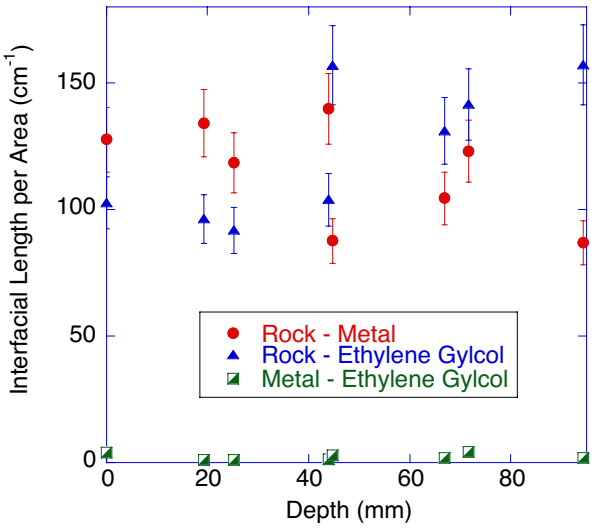

Figure 22. Interfacial length per area as a function of depth for sample 5a.

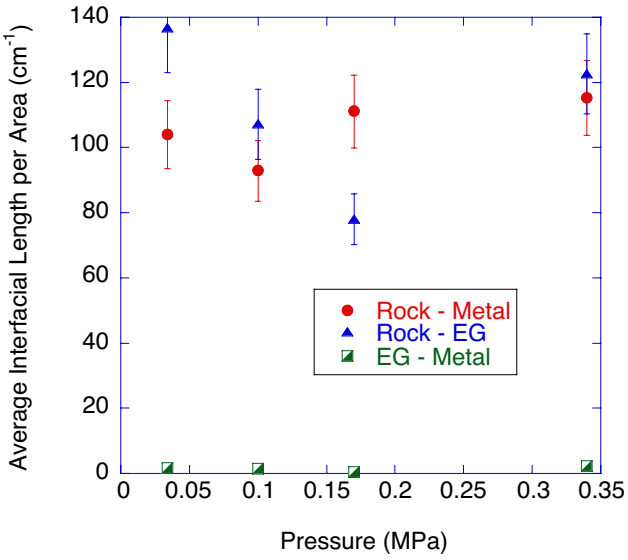

Figure 23. Interfacial length per area as a function of injection pressure for the samples listed in Table 1.

4.0 Conclusions and Future Work

4.1 Optical Coherence Imaging

Holograms acquired using optical coherence imaging provide information on the thickness of the grains (from reflections from the top and bottom surfaces of the grains) and on the geometry of the grains (from reflections from the side facets of the grains). From stacked (serial) holograms, the geometric shapes of several sand grains can be delineated. Interfaces between grains and pores was acquired for depths as greater a half a millimeter beneath the surface of the sample. Imaging the sandstone in the dry condition and in the water saturated condition enables identification of the pore space in the holograms.

Future work will include additional experiments with and without the sandstone saturated with refractive index match fluids to determine if the depth resolution of OCI can be increased. Work will begin on design of OCI to work with an optical fiber bundle for use in simulated boreholes in the laboratory.

4.2 Micro-Models

Ours are the first experimental measurements of P_{cap}, S and IAV in any system. The use of micro-models in this work was essential, since with most experimental systems it is not possible to obtain high quality images (required to measure IAV) of the multiple phases *in-situ* . Our central result is that the variables P_{cap}, S and IAV are sufficient to provide a complete description of multiphase flow. This result is in agreement with the general theoretical arguments of Gray and coworkers (Gray 1983, Muccino et al. 1998), and with the numerical simulations of Reeves and Celia (1991). Much work remains to be done. Our results along with the theory just cited indicates that a description of multiphase flow must include all three variables P_{cap}, S and IAV . We now have a substantial body of data on the actual functional form of the P_{cap}-S-IAV relation. Theoretical means to calculate this

relationship, and also compute additional quantities such as the flow rate, must still be developed. Our results will provide strong tests of these theories.

4.3 Wood's Metal Method

Homogeneity of interfacial length per area in the direction perpendicular to injection axis for a given pressure was observed. Determination of homogeneity enables the use of short samples to probe ILA at low injection pressures. If it is determined that a unique relationship exists for ILA, capillary pressure and saturation for natural three-dimensional systems (e.g., sandstone), then ILA provides a natural yard-stick for defining the role of scale in multiphase fluid properties of porous media.

Our future work will be the measurement of IAV on sandstone for low values of capillary pressures, i.e. pressures one-tenth or less of those used so far in this study. This pressure range is important to obtain pore saturations that are less than 80%. This will require a slight modification to the injection system and the sample preparation technique (both for injection and scanning electron microscopy).

5.0 References

Agrawal, D. L. et al., The Effect of Percolating Structure on The Petrophysical Properties of Berea Sandstone, Rock Mechanics as a Multidisciplinary Science, p345-354, 1991

Darcy, H., Determination of the laws of flow through sane, Les fontaines publiques de la ville de Dijon, Victor Dalmont, Paris, 1856, 590-594, (translated and reprinted in Physical Hydrology, edited by R. A. Freeze and W. Back, Hutchinson Ross Publishing Company, Stroudsburg, PA, 1983).

Giordano, N., and J. T. Cheng, Microfluid mechanics: Progress and opportunities, J. Phys. Condensed Matter, **13**, R271 (2001).

Giordano, N., and J. T. Cheng, Interfacial Area, Pore Geometry and Hydraulic Properties from Micro-Models, Milestone Report (DOE Award De-AC26-99BC15207), Purdue University, March 2001.

Gray, W. G., General conservation equations for multi-phase systems: 4. Constituitive theory including phase change, Adv. Water Resources **6**, 130-140 (1983).

Gray, W. G. (private communication, 1998).

Hassanizadeh, S. M. and W. G. Gray, General conservation equations for multi-phase systems: 1. Averaging procedure, Adv. Water Resources **2**, 131-144 (1979).

Hassanizadeh, S. M. and W. G. Gray, Mechanics and thermodynamics of multiphase flow in porous media including interphase boundaries, Water Resource Research **13**, 169-186 (1990).

Muccino, J. C., Gray, W. G. and L. A. Ferrand, Toward and improved understanding of multiphase flow in porous media, Rev. Geophys. **36**, 401 (1998).

Nolte, D.D, and L. J. Pyrak-Nolte, Stratified continuum percolation: Scaling geometry of hierarchical cascades, Phys. Rev. A **44**, 6320 (1991).

Nolte, D. D. ,"Photorefractive Effects and Materials,", (Kluwer Academic Publishers, Dordrecht, 1995).

Reeves, P. C. and M. A. Celia, A functional relationship between capillary pressure, saturation, and interfacial area as revealed by a pore-scale network model, Water Resource Research **32**, 2345 (1996).

Shipley Microelectronic Product Guide, Shipley Co., Newton, MA, 1982

Thompson, L.F., C.G. Willson, and M.J. Bowden, Introduction to Microlithography, 2nd edition, American Chemical Society, Washington, DC, 1994